Title	Fixed-mesh approach for different dimensional solids in fluid flows : application to biological mechanics
Author(s)	Miyauchi, Suguru; Ito, Azusa; Takeuchi, Shintaro; Kajishima, Takeo
Citation	Journal of Mechanical Engineering and Sciences. 6 P.818-P.844
Issue Date	2014-06
Text Version	author
URL	http://hdl.handle.net/11094/71460
DOI	
rights	This article is licensed and distributed under the terms of the Creative Commons Attribution-Non-Commercial 4.0 International License.
Note	

Osaka University Knowledge Archive : OUKA

https://ir.library.osaka-u.ac.jp/repo/ouka/all/

Osaka University

Fixed-mesh approach for different dimensional solids in fluid flows: application to biological mechanics

Suguru MIYAUCHI [1,2], Azusa ITO [1], Shintaro TAKEUCHI [1] and Takeo KAJISHIMA [1]

[1] Department of Mechanical Engineering, Osaka University,
2-1 Yamada-oka, Suita, Osaka 565-0871, Japan

Abstract

For simulations of biological flows, our original immersed solid method and feedback immersed boundary method are coupled to deal with the interaction between a fluid and solids of different dimensional topologies. The mesh used in both methods is non-conforming with respect to the fluid-solid interface, and the coupled approach facilitates the handling of the fluid-structure interaction including large deformation of the solids. We show the validity of our method through simulations of static and dynamic benchmark problems. The results of the simulations confirmed that our method has a first order accuracy and shows good agreement with the strong coupling method reported in the literature. As for examples of biological flow, the expiratory flow through vocal cords and pulsative flow through an elastic channel with fibers are analyzed. For the flow through vocal cords, the vocal cords exhibit different vibration modes depending on the initial clearance of the vocal cords, regardless of the contacts of the vocal cords. For the flow through the elastic channel with fibers, fibers decrease the wall shear stress, and the elasticity of the wall enhances the reduction of the wall shear stress.

1   Introduction

In recent years, numerical simulations of fluid-structure interaction (FSI) have been performed for designing industrial devices and understanding phenomenon of life activities. Numerical analysis of biological FSI is particularly challenging as it involves large deformation of biological tissues of complex geometry and moving boundary problems. In many cases, motions of a fluid and solid are described in Eulerian and Lagrangian frames, respectively, due to their constitutive laws, which often causes a difficulty in coupling the different notational systems in FSI. The simulations become even more complex when including solids of different dimensional topologies (such as fibers, membranes and three dimensional solids) of arbitrary shapes, particularly in biological problems.

     Numerical methods are separated into two types in terms of computational mesh; approaches employing body-conforming mesh and non-conforming mesh regardless of the geometry of the solids.

---

[2]Research Fellow of the Japan Society for the Promotion of Science (DC2)

Examples of the former type include arbitrary Lagrangeian-Eulerian (ALE) methods (Bathe et al. 1995; Gao and Hu 2009; Sawada and Hisada 2007) and deforming spatial domain/stabilized space-time (DSD/SST) method (Tezduyar et al. 1992a,b; Tezduyar 1992; Tezduyar et al. 2006; Hübner et al. 2004; Zilian and Legay 2008). In those methods, fluid motion is resolved by keeping the grid points dense near the interface, and by taking the advantage of body fitted mesh, the methods were applied to a number of problems. By employing a monolithic approach, computational stability is strengthened as the interfacial velocity and the stress conditions are strictly satisfied (Zhang and Hisada 2004). However, because a monolithic integration of the fluid and solid solvers is needed, selectivity of the numerical approaches is rather limited. Furthermore, generating mesh around multiple objects is not straightforward, and the simulations become more difficult when the geometrical topology changes in association with contacting and fragmentation of the solids. In the non-conforming mesh methods, on the other hand, an easily-prepared fixed mesh or fixed Cartesian mesh can be used even if the interface geometry becomes complex. Although the boundary layer around the object is not resolved as finely as the body-conforming mesh, by taking the advantage of the efficiency in computation, various methods using non-conforming mesh have been developed, and many improvements were proposed.

Immersed boundary method (IBM) (Peskin 1997, 2002; Mittal and Iaccarino 2005; Kim and Peskin 2006) is one of the notable methods for solving FSI problems among the non-conforming mesh methods. In this method, the fluid and solid are coupled by communicating the quantities in Eulerian and Lagrangian frames. Specifically, the velocity interpolation from the ambient fluid frame to the solid frame and distribution of the elastic force acting on the solid to the ambient fluid are performed by using an approximate delta function. Also a number of new ideas for the approximate delta function and time marching scheme have been proposed for improving the interface conditions (Peskin and Printz 1993; Mori and Peskin 2008; Stockie 1997). Later, Goldstein et al. (1993) proposed a feedback forcing immersed boundary method by introducing a feedback loop for reducing the velocity difference between the fluid and solid with two empirical parameters (physically equivalent to the effects of a spring and dashpot) in the momentum forcing term. However, by employing large values for the parameters for imposing the no-slip condition, the time increment must comply with strict conditions (Goldstein et al. 1993; Huang and Sung 2009).

The distributed Lagrange multiplier/fictitious domain (DLM/FD) method (Glowinski et al. 1999; Baaijens 2001) is an advanced idea about momentum forcing and is formulated based on the Lagrange multiplier method to satisfy the no-slip condition. The Lagrange multipliers, which are equivalent

to surface forces, work to satisfy the kinematic condition at the interface by introducing in the equations of motion of both phases. This method offers high computational stability when the monolithic approach is employed, and a relatively large time increment is available (Sawada et al. 2008). However, because the discontinuity in the velocity gradient at the interface is not considered, a non-physical velocity field arises in the vicinity of the interface (Van et al. 2004). In recent years, DLM/FD method with extended finite element method (XFEM) (Moës et al. 1999; Belytschko and Black 1999) is proposed to overcome this drawback (Gerstenberger and Wall 2008).

In immersed interface method (IIM) (Lee and LeVeque 2003; Wiegmann and Bube 2000; Li 1994, 1997; Xu and Wang 2006), the interaction between the fluid and solid is formulated with no momentum forcing. Instead, a discontinuity at the interface is taken into account in its finite-difference formulae for describing the interaction between the fluid and solid. A second order accuracy in space is achieved with no use of an approximate delta function.

Note that the objects employed in IBM and IIM are fiber-like or membrane-like elastic (sometimes, closed) structures. Those objects are discretized with Lagrange markers placed on the objects surface, and the interaction with the surrounding fluid is solved by finite difference method. On the other hand, DLM/FD method is capable of dealing with the interaction between fluid and rigid objects with a finite volume or thin elastic objects (such as fibers and membranes). Further advanced ideas for treating an elastic solid object with a finite volume are found in immersed finite element method (Zhang et al. 2004) and extended immersed boundary method (Wang and Liu 2004) by incorporating finite element analysis for deformation of the solid objects. Those methods also employ Lagrangian points within the solid objects, and for interpolation and distribution between the Eulerian and Lagrangian meshes, a convolution method with a kernel function on an unstructured mesh was developed (Liu et al. 1995).

Full Eulerian method solves both motions of the fluid and solid in an Eulerian frame. In the method proposed by Dunne and Rannacher (2006), governing equations of the fluid and solid are integrated by treating a displacement field in the Eulerian frame. From the values of the displacement field, the fluid and solid are distinguished as in a level set method. A similar idea was implemented by Cottet et al. (2008). To obtain the displacement field in Eulerian frame, a convective equation of the set of initial positions described in Eulerian frame is solved. On the other hand, in the full Eulerian method proposed by Sugiyama et al. (Sugiyama et al. 2010, 2011; Ii et al. 2011; Nagano et al. 2010), the presence of the solid is expressed by a volume fraction, and the stress of the entire domain is given by the weighted average of volume fraction. The convective equation of the volume

fraction and the transportation equation of left Cauchy-Green deformation tensor are solved as well as the equations of motions. Later, this method was extended to treat membrane structures (Ii et al. 2012a,b), and applied to a pipe flow including a number of blood cells.

Kajishima and co-workers proposed an original immersed solid method (Kajishima et al. 2001, 2002), and the method was extended for FSI problems (Yuki et al. 2007; Takeuchi et al. 2010). In this method, the fluid and solid phases are discretized by finite difference and finite element methods, respectively. Momentum forcing is formulated with a volumetric average velocity of the fluid and solid. The geverning equations of the fluid are solved assuming that the entire computational domain is occupied by a fluid. After that, the velocity field in the solid-occupying region is replaced by the solid velocity. The interaction force is modeled to be proportional to the local solid volume fraction and the velocity difference between the fluid and solid in order to impose the no-slip condition at the interface. This method was applied to a flow field with a number of rigid particles (Kajishima et al. 2001, 2002) and elastic particles (Takeuchi et al. 2010), and good computational efficiency has been demonstrated. Due to the employment of a finite element approach for solving the solid deformation, it is advantageous that some well-established ideas and algorithms are readily incorporated such as contact algorithm and solid incompressibility by using the Lagrange multiplier method.

A number of methods for hybrid Eulerian-Lagrangian FSI simulation have been formulated based on the interpolation and distribution operations for communicating between the Eulerian and Lagrangian frames. However, updating the solid points by using the interpolated velocities causes computational instability as the equilibrium state within the solid object is not guaranteed (Sawada et al. 2008). On the other hand, in our immersed solid method, the deformation of the solid is calculated by solving the equation of motion with the interaction force. Therefore, the equilibrium state is maintained at every time step, resulting in a non-sensitive method to the instability caused by the fluid motion.

In this paper, we attempt a new approach for FSI problems including objects of different dimensional topologies (e.g., fiber, membrane and elastic solid object with a finite volume), and demonstrate some examples of the biological problems. Until now, few analyses of the interactions between the fluid and combined solids of different dimensional topologies have been conducted as different numerical treatments are needed for solving the motion of those objects in a fluid. In this study, solid objects are represented in a Lagrangian way to facilitate the contact analysis by handling the fluid-solid interface explicitly and the coupling with solids of different dimensional topologies. We improve the immersed solid method to allow large deformation of the solid object by considering geometrical

nonlinearity of the solid. The validity of our method is shown by solving some benchmark problems. The method is applied to the biological FSI problems such as a flow through a constricted elastic channel and a flow through elastic walls covered with fiber structures. Those examples are simplified cases of vocal cords vibration in an air way and sugar-fibers (glycocalyx) in a blood vessel. In the analysis of the flow through the vocal cords, topology change takes place when the vocal cords are in contact. The effect of the contact on the vocal cords vibration induced by the fluid flow is studied. For the interaction between the fluid and fiber-like structures, the influences of the glycocalyx and elasticity of the vessel wall on the flow field are investigated. Through the numerical examples, we show the versatility and robustness of our method to the biological flow.

2   Governing equations

2.1   Fluid flow

The fluid is assumed to be incompressive Newtonian fluid. The governing equations are the continuity equation and Navier-Stokes equation:

$$\nabla \cdot \boldsymbol{u}_f = 0, \tag{1}$$

$$\rho_f \left(\frac{\partial \boldsymbol{u}_f}{\partial t} + \boldsymbol{u}_f \cdot \nabla \boldsymbol{u}_f \right) = -\nabla p + \mu_f \nabla^2 \boldsymbol{u}_f, \tag{2}$$

where $\boldsymbol{u}_f$ denotes the fluid velocity, p the static pressure, ρ_f the fluid density, μ_f the viscosity.

2.2   Elastic body

A variational problem is formulated for the motion of the elastic solid including the contact between the solids based on the Lagrange multiplier method. The potential energy of elastic body Π is given as

$$\Pi = \frac{1}{2} \int_{V_0} (\boldsymbol{S} : \boldsymbol{E} - \rho_s \boldsymbol{b} \cdot \boldsymbol{z}) \, dV - \int_S \boldsymbol{t} \cdot \boldsymbol{z} dS + \boldsymbol{\lambda} \cdot \boldsymbol{c}, \tag{3}$$

where ρ_s denotes the density at reference configuration, V_0 the volume at reference configuration, S the current surface, $\boldsymbol{E}$ the Green-Lagrange strain, $\boldsymbol{S}$ the second Piola-Kirchhoff stress tensor, $\boldsymbol{b}$ the body force, $\boldsymbol{t}$ the surface force, $\boldsymbol{z}$ the displacement, $\boldsymbol{\lambda}$ the Lagrange multiplier, $\boldsymbol{c}$ the constraint equation of the contact. Assuming that there are two bodies and $\boldsymbol{x}_s^i \; (i = 1, 2)$ are position vectors on the contacting two surfaces, the constraint equation is expressed as follows (Wriggers 2006):

$$\boldsymbol{c} = \begin{cases} \boldsymbol{x}_s^2 - \boldsymbol{x}_s^1 & \text{if } (\boldsymbol{x}_s^2 - \boldsymbol{x}_s^1) \cdot \boldsymbol{n}_1 < 0, \\ \boldsymbol{0} & \text{otherwise,} \end{cases} \tag{4}$$
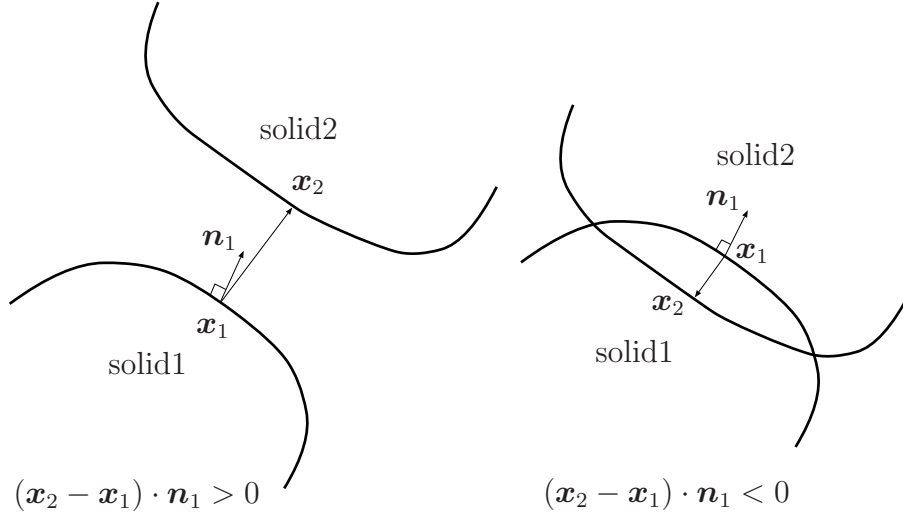
Figure 1: Typical two patterns of arrangements of two objects. When $(\boldsymbol{x}_2 - \boldsymbol{x}_1) \cdot \boldsymbol{n}_1$ is positive, two objects do not overlap. When $(\boldsymbol{x}_2 - \boldsymbol{x}_1) \cdot \boldsymbol{n}_1$ is negative, two objects overlap.

where $\boldsymbol{n}_1$ is the outward normal vector at $\boldsymbol{x}_s^1$. An arrangement of the two objects and a judgment of the contact are illustrated in Fig.1. The following equation is obtained from the first variation ($\delta\Pi = 0$) and by substituting $\boldsymbol{b} = -\boldsymbol{f}_s - \partial^2\boldsymbol{z}/\partial t^2$ and $\boldsymbol{t} = 0$ (in this paper, the interaction force are modeled to be a body force.):

$$\int_{V_0} \rho_s \frac{\partial^2 \boldsymbol{z}}{\partial t^2} \cdot \delta\boldsymbol{z} dV + \int_{V_0} \boldsymbol{S} : \delta\boldsymbol{E} dV + \boldsymbol{\lambda}\frac{\partial \boldsymbol{c}}{\partial \boldsymbol{z}}\delta\boldsymbol{z} + \boldsymbol{c} \cdot \delta\boldsymbol{\lambda} = -\int_{V_0} \rho_s \boldsymbol{f}_s \cdot \delta\boldsymbol{z} dV. \tag{5}$$

In the present study, St.Venant-Kirchhoff material and neo-Hookean material are used for the elastic objects. The constitutive law of those materials is given as the following strain energy density functions, respectively:

$$W_{SK} = \frac{\lambda}{2}(\mathrm{tr}\boldsymbol{E})^2 + \mu\mathrm{tr}\boldsymbol{E}^2, \tag{6}$$

$$W_{NH} = \frac{G}{2}\left(\mathrm{tr}\hat{\boldsymbol{C}} - 2\right) + \frac{K}{2}(J - 1)^2, \tag{7}$$

$$\hat{\boldsymbol{C}} = J^{-2/3}\boldsymbol{F}^T\boldsymbol{F},$$

where λ, μ are Lamé constants, G, K the transverse elasticity modulus, the bulk modulus, respectively, $\boldsymbol{F}$ the deformation gradient tensor and J is Jacobian defined as $J = \det\boldsymbol{F}$. The second Piola-Kirchhoff stress tensor is obtained from the strain energy density function W as follows:

$$\boldsymbol{S} = \frac{\partial W}{\partial \boldsymbol{E}}. \tag{8}$$

2.3   Fiber

The motion of a fiber is determined by the following equation:

$$\rho_f' \frac{\partial^2 \boldsymbol{x}_f}{\partial t^2} = \frac{\partial}{\partial s}\left(T\frac{\partial \boldsymbol{x}_f}{\partial s}\right) - \frac{\partial^2}{\partial s^2}\left(\gamma_f \frac{\partial^2 \boldsymbol{x}_f}{\partial s^2}\right) - \boldsymbol{F}_f + \boldsymbol{F}_r, \tag{9}$$

where ρ_f' is the density difference between the fiber and the surrounding fluid, $\boldsymbol{x}_f$ a Lagrangian position on the fiber, s the arclength, γ_f the bending stiffness, $\boldsymbol{F}_f$ the interaction force acting on the fiber from the fluid. Tension T works to satisfy the inextensibility condition:

$$\frac{\partial \boldsymbol{x}_f}{\partial s} \cdot \frac{\partial \boldsymbol{x}_f}{\partial s} = 1. \tag{10}$$

To avoid the overlap between the fibers, the following repulsive force $\boldsymbol{F}_r$ is introduced as an external force term in Eq.(9):

$$\boldsymbol{F}_r = -\frac{\partial W_r}{\partial \boldsymbol{x}_f}, \tag{11}$$

$$W_r = \frac{1}{2}k\frac{1}{|\boldsymbol{x}_f - \boldsymbol{x}_f'|^2} \quad \text{if} \quad |\boldsymbol{x}_f - \boldsymbol{x}_f'| < \frac{1}{2}\Delta x. \tag{12}$$

where Δx is a grid width for a fluid domain.

3   Numerical methods

3.1   Discretization

3.1.1   Fluid flow

The whole computational domain is divided into fixed uniform rectangular cells, unless specified otherwise. Eqs.(1) and (2) are discretized by a finite difference method.

Interaction terms with solid and fiber are incorporated into a discretized equation of Eq.(2):

$$\rho_f \frac{\delta \boldsymbol{u}_f}{\delta t} = -\rho_f \boldsymbol{u}_f^n \cdot \nabla \boldsymbol{u}_f^n - \rho_f \nabla p^n + \mu_f \nabla^2 \boldsymbol{u}_f^n + \boldsymbol{f}_s + \boldsymbol{f}_f , \tag{2'}$$

where $\delta/\delta t$ is the discretization operator in time, the subscript n indicates the time level, $\boldsymbol{f}_s$ is the interaction force between the fluid and solid with a finite volume and $\boldsymbol{f}_f$ is the interaction force between the fluid and fibers. The models of $\boldsymbol{f}_s$ and $\boldsymbol{f}_f$ are described later.

A fractional step method is employed for coupling the velocity and pressure. For spatial discretization, the variables are arranged on the collocated points, and the central finite difference scheme of a 2nd order accuracy is applied. For the time advancement, the 2nd order Adams-Bashforth method is applied for the convective and viscous terms.

3.1.2 Elastic body

Spatial discretization of Eq.(5) is performed by a finite element method with linear triangular elements. The Newmark-β method considering the effect of the contact force (Wriggers 2006) is applied for the time advancement:

$$
\boldsymbol{z}^{n+1} = \boldsymbol{z}^n + \Delta t \dot{\boldsymbol{z}}^n + \frac{\Delta t^2}{2}\left[(1-2\beta)\,\boldsymbol{a}_{int}^n + 2\beta \boldsymbol{a}_{int}^{n+1}\right] + \frac{\Delta t^2}{2}\boldsymbol{a}_{con}^{n+1}, \tag{13}
$$

$$
\dot{\boldsymbol{z}}^{n+1} = \dot{\boldsymbol{z}}^n + \Delta t\left[(1-\gamma)\,\boldsymbol{a}_{int}^n + \gamma \boldsymbol{a}_{int}^{n+1}\right] + \Delta t\boldsymbol{a}_{con}^{n+1}, \tag{14}
$$

where

$$
\boldsymbol{a}_{int} = \boldsymbol{M}^{-1}\left(\boldsymbol{F} - \boldsymbol{Q}\right), \tag{15}
$$

$$
\boldsymbol{a}_{con} = \boldsymbol{M}^{-1}\boldsymbol{F}_{con}. \tag{16}
$$

Here $\boldsymbol{z}$ is displacement, β and γ the parameters for the time marching, and $\boldsymbol{M}$, $\boldsymbol{F}$, $\boldsymbol{Q}$ and $\boldsymbol{F}_{con}$ the mass matrix, the external force vector, the internal force vector and the contact force vector, respectively. The superscripts represent the time levels. In this study, $\beta = 1/4$ and $\gamma = 1/2$ are employed. Note that the external force ($\boldsymbol{F}$) is a sum of the contributions of fluid and fibers ($\boldsymbol{F}_s$ and equivalent nodal forces described in Section 3.2.3) and those are explained later.

3.1.3 Fiber

The fibers are constructed with sets of Lagrangian markers. By following Huang et al. (2007), the tension along the fiber is determined implicitly so as to satisfy the inextensibility condition, Eq.(10).

By differentiating Eq.(9) with respect to s and multiplying $\partial \boldsymbol{x}_f/\partial s$, the following pseudo-Poisson equation for T is obtained:

$$
\frac{\partial \boldsymbol{x}_f}{\partial s} \cdot \frac{\partial^2}{\partial s^2}\left(T\frac{\partial \boldsymbol{x}_f}{\partial s}\right) = \frac{\rho_f'}{2}\frac{\partial^2}{\partial t^2}\left(\frac{\partial \boldsymbol{x}_f}{\partial s}\cdot\frac{\partial \boldsymbol{x}_f}{\partial s}\right) - \rho_f'\frac{\partial^2 \boldsymbol{x}_f}{\partial t\partial s}\cdot\frac{\partial^2 \boldsymbol{x}_f}{\partial t\partial s}
$$
$$
-\frac{\partial \boldsymbol{x}_f}{\partial s}\cdot\frac{\partial}{\partial s}\left(-\frac{\partial^2}{\partial s^2}\left(\gamma_f\frac{\partial^2 \boldsymbol{x}_f}{\partial s^2}\right) - \boldsymbol{F}_f + \boldsymbol{F}_r\right). \tag{17}
$$

Eq.(10) is substituted for the discretized equation of Eq.(17), and Eqs.(9) and (17) are solved by a finite difference method. With the obtained tension, the equation of motion for the fibers (Eq.(9)) is solved for updating the positions of the Lagrange markers. The details of the discretization are found in Huang et al. (2007).

3.2 Interaction Model

Interactions between the fluid, elastic bodies and fibers are treated by coupling three models obtained from two-body problems.

3.2.1 Interaction between fluid and elastic body: Immersed solid method

A unified velocity field is defined by the volumetric average of the fluid velocity $\boldsymbol{u}_f$ and solid velocity $\boldsymbol{u}_s(= \partial \boldsymbol{z}/\partial t)$:

$$\boldsymbol{u} = (1 - \alpha)\boldsymbol{u}_f + \alpha\boldsymbol{u}_s, \tag{18}$$

where α denotes the volumetric fraction of the solid phase in a control volume. The interaction term $\boldsymbol{f}_s$ in Eq.(2′) is modeled to achieve the velocity field Eq.(18). Discretizing the first term in the left hand side of Eq.(2′) with respect to t yields

$$\rho_f \frac{\boldsymbol{u}_f^{n+1} - \tilde{\boldsymbol{u}}_f}{\Delta t} = \boldsymbol{f}_s, \tag{19}$$

where Δt is the time increment. Intermediate velocity $\tilde{\boldsymbol{u}}_f$ is obtained by solving the basic equations of the fluid:

$$\tilde{\boldsymbol{u}}_f = \boldsymbol{u}_f^n + \int_{t^n}^{t^{n+1}} \frac{1}{\rho_f} \left(-\rho_f \boldsymbol{u}_f \cdot \nabla \boldsymbol{u}_f - \nabla p + \mu_f \nabla^2 \boldsymbol{u}_f + \boldsymbol{f}_f \right) dt, \tag{20}$$

assuming that the entire computational domain is occupied by the fluid. From the request that $\boldsymbol{u}_f^{n+1}$ in Eq.(19) is consistent with Eq.(18), the interaction term $\boldsymbol{f}_s$ is given as follows:

$$\boldsymbol{f}_s = \rho_f \frac{\alpha(\boldsymbol{u}_s - \tilde{\boldsymbol{u}}_f)}{\Delta t}. \tag{21}$$

The counteracting force acting on the solid from the fluid is obtained by numerically integrating $\boldsymbol{f}_s$ over the solid volume:

$$\boldsymbol{F}_s = \rho_s \int_{V_e} N^T \left(-\boldsymbol{f}_s \right) dV, \tag{22}$$

where N is the shape function and V_e is the volume of the solid element.

3.2.2 Interaction between fluid and fiber: Feedback immersed boundary method

For the interaction between the fluid and fibers, a model proposed by Huang and Sung (2009) is introduced. By integrating the Goldstein's feedback force (Huang and Sung 2009), the interaction force acting on the fibers from the fluid is given by the following equation:

$$\boldsymbol{F}_f = \kappa \left(\boldsymbol{x}_{f,ib}^{n+1} - 2\boldsymbol{x}_f^n + \boldsymbol{x}_f^{n-1} \right), \tag{23}$$

where κ is a penalty parameter of a large value, $\boldsymbol{x}_{f,ib}$ is the predicted position calculated by the following operation:

$$\boldsymbol{x}_{f,ib} = \boldsymbol{x}_f + \int_\Omega \boldsymbol{u}_f \delta \left(\boldsymbol{x}_f - \boldsymbol{x} \right) d\boldsymbol{x} \Delta t. \tag{24}$$
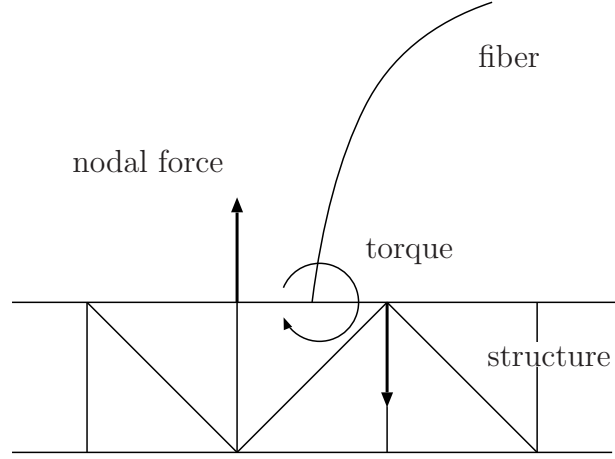
Figure 2: The torque acting on the elastic body from the fiber and the equivalent nodal forces.

Here, Ω is a fluid domain and δ is an approximate delta function. In the present study, the same form of the approximate delta as Peskin (1997) is employed. The same approximate delta function is also used for the interpolation of the velocity from the ambient fluid to the solid point and distribution of the internal force to the fluid phase as follows:

$$\boldsymbol{f}_f = \int_\Gamma \boldsymbol{F}_f \delta\left(\boldsymbol{x} - \boldsymbol{x}_f\right) ds. \tag{25}$$

Here Γ is a line along the fiber.

3.2.3   Interaction between elastic body and fiber

In the present work, the fibers are clamped on the surface of the elastic body, and a simple procedure for satisfying the interface condition is introduced; the geometrical condition is given only to the fibers assuming that inertia of the fiber is small compared with that of the elastic body. Therefore, the bottom end of the fibers is enforced to be attached to the surface of the elastic body. On the other hand, the dynamic condition is given only to the elastic body. Under this decoupled calculation, if the fiber receives a fluid force in the normal direction to the fiber axis, the elastic body experiences the torque. Therefore, by calculating the equivalent nodal forces to the torque acting on the solid body, the forces are added as external forces to the discretized equation of the elastic body. Figure 2 shows the schematic of the torque from the fiber and the nodal force.

3.3   Calculation procedure

The calculation procedure is summarized as follows:

1. Interaction forces between the fluid and fibers are computed using the approximate delta function.

2. In the whole computational domain as a fluid, $\tilde{\boldsymbol{u}}_f$ is obtained by Eq.(20).

3. $\tilde{\boldsymbol{u}}_f$ is replaced with the volumetric averaged velocity in Eq.(18), and interaction force $\boldsymbol{f}_s$ is calculated.

4. Calculating the external vector composed of $\boldsymbol{F}_s$ and the torque from the fibers, the positions, velocities and accelerations of elastic bodies are updated by solving the equation of motion (Eq.(5)).

5. Solving Eq.(17), the tension under the inextensibility condition is obtained, and the positions of the fibers are updated by solving the equation of motion (Eq.(9)).

The above loop is repeated.

4   Validation

Though some three-dimensional FSI problems have been attempted with the present method, only two-dimensional problems are dealt with in this paper. Therefore, numerical results of two dimensional validation problems are shown here.

4.1   Flow through the elastic wavy channel

To assess the validity of the numerical method for the deformation of the elastic bodies by the fluid force, the problem proposed by Nagano et al. (2010) is attempted, and the convergence rate of our method with respect to the grid size is examined. The computational domain is illustrated in Fig.3. As for the boundary condition for the fluid phase, the no-slip condition is applied to the upper and lower boundaries (($\forall x, y = H$) and ($\forall x, y = 0$), respectively), and the left and right boundaries (($x = 0, \forall y$) and ($x = L, \forall y$), respectively) are periodic. For the solid phase, the displacements on the upper and lower boundaries are fixed and are periodic on the left and right boundaries. A neo-Hookean material is assumed for the elastic objects. This material shows incompressibility, and this nature is necessary for constructing a theoretical profile (Nagano et al. 2010) of the deformed interface. The fluid is driven by a pressure gradient in the x-direction. In this problem, all the variables are dimensionalized. Two sets of the geometrical parameters are employed; $(H, h, \delta, L) = (4, 2, 0.3, 6)$ is referred to as Case 1 and $(H, h, \delta, L) = (3, 1, 0.2, 6)$ as Case 2. The computational condition is summarized in Tab.1. Five different spatial resolutions are tested for the fluid phase, and the resolution of the solid object is increased according to the fluid mesh.

Figure 4 shows the interface profiles at the initial condition and steady state for both cases. The
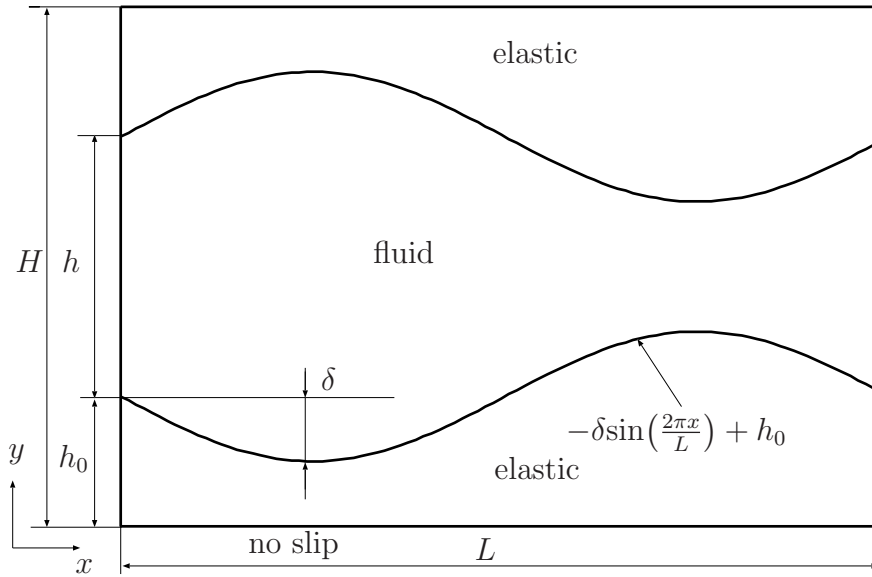
Figure 3: Schematic of the wavy elastic channel.
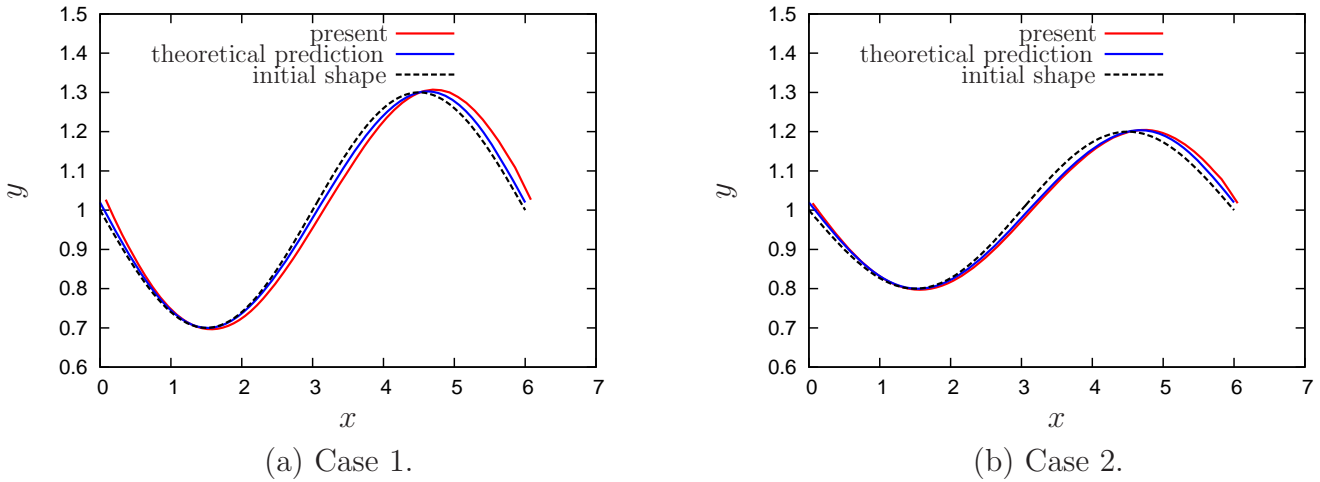

(a) Case 1.

(b) Case 2.

Figure 4: Comparison of the interface profiles between the simulation results and the theoretical analysis.

results are also compared with the theoretical prediction of Nagano et al. (2010), which is derived under the assumptions of $h \ll L$ and $\delta \ll 1$. Case 2 is closer to the assumption than Case 1, and the results show a tendency that our solution approaches to the theoretical solution as the geometrical condition is closer to the assumption.

We also investigate the convergence rate of our method. The differences are evaluated in L_2 and L_∞ norms, based on the result conducted with the number of grid points 192×96 in Case 2. The tendencies of the convergence of the difference in L_2 and L_∞ are shown Fig.5. The differences monotonously decrease approximately at a first order rate in both norms. Therefore, the solution converges to a unique solution as the number of grid points is increased.

Table 1: Simulation conditions for the flow through the elastic wavy channel.

fluid	Density	ρ_f	1
	Viscosity	μ_f	1
	Constant pressure gradient	$-\nabla p_c$	1
elastic body	Density	ρ_s	1×10^1
	Shear modulus of rigidity	G	1×10^1
	Bulk modulus	K	1×10^3
numerical parameter	Time increment	Δt	5×10^{-4}
	Number of grid points for fluid	$N_x \times N_y$	48×24 64×32 96×48 128×64 192×96
	Numbers of nodes and elements for solid	N_n, N_e	882, 1536 1430, 2560 3298, 6144 5934, 11264 12738, 24576

4.2　Vibration of elastic bar due to the fluid force

A benchmark problem proposed by Turek and Hron (2006) is solved to assess the validity of the dynamic deformation behavior of the elastic object excited by the fluid force. A computational target is an elastic bar vibrating in a flow with one end attached to a fixed rigid cylinder. A St.Venant-Kirchhoff material is assumed for the elastic bar. The computational domain and boundary condition are shown in Fig.6. To match the condition to Turek and Hron (2006), the size of the computational domain is $L = 2.5[\mathrm{m}]$ and $H = 0.41[\mathrm{m}]$. The center of the cylinder is placed at $(x, y) = (0.2[\mathrm{m}], 0.2[\mathrm{m}])$. The radius of the cylinder is $r = 0.05[\mathrm{m}]$. The size of the elastic bar is $\ell = 0.35[\mathrm{m}]$ and $h = 0.01[\mathrm{m}]$. The no-slip condition is applied at the upper and lower boundaries of the domain, and a convective outflow condition is imposed at the outflow boundary. The inflow velocity is given as follows:

$$v_{in}(t, y) \ [\mathrm{m/s}] = \begin{cases} \hat{v}(y) \dfrac{1 - \cos{(\pi t/2)}}{2} & (t < 2.0 \ [\mathrm{s}]), \\ \hat{v}(y) & (t \geq 2.0 \ [\mathrm{s}]), \end{cases} \tag{26}$$

$$\text{where} \qquad \hat{v}(y) = \frac{3}{2}\bar{U}\frac{y\,(H - y)}{(H/2)^2}. \tag{27}$$

The simulation conditions are summarized in Tab.2.

　　Figure 7 shows a snapshot of the deformed object and a contour of the pressure field. The elastic bar is deformed largely by the fluid force, and vortices are discharged behind the bar. This
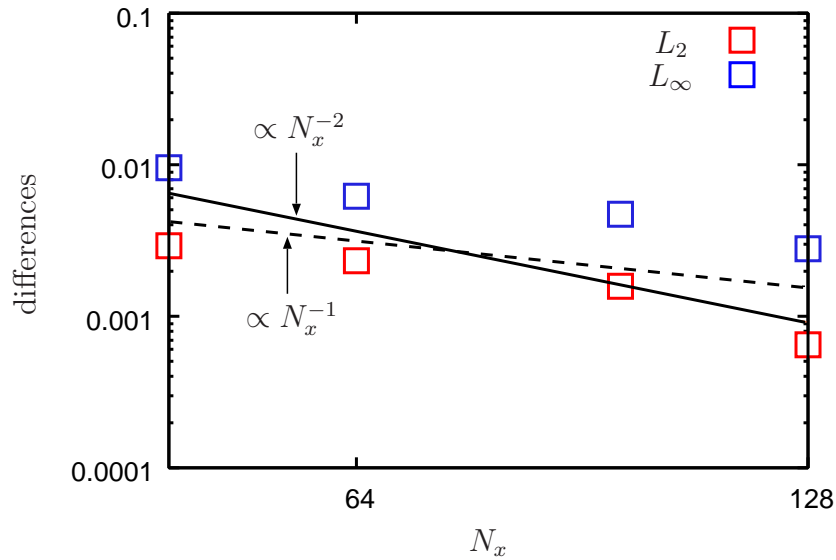
Figure 5: The differences of the interface profile in L_2 and L_∞ norms versus the number of grid points N_x.
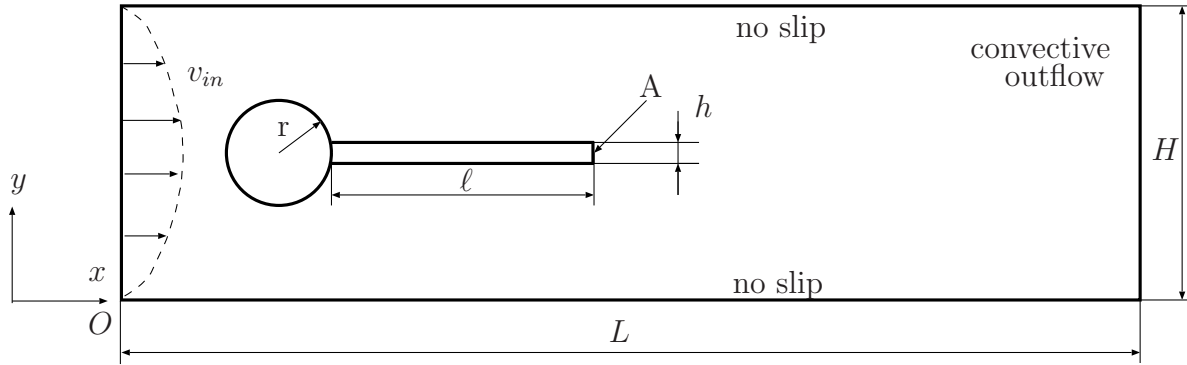

Figure 6: The computational domain for the flow around the elastic bar attached to the rigid cylinder.

aspect of the flow field agrees qualitatively well with the observation of Heil et al. (2008). The displacement of Point "A" (the free end of the elastic bar, see Fig.6) in the y-direction during the initial development stage is shown in Fig.8 together with the result of Dunne and Rannacher (2006). Our result shows good agreement. To see the oscillating behavior of the elastic bar, Fig.9 shows the Fourier coefficient of the time series of the y-displacement at Point "A" at quasi-steady state. The difference in frequencies of the dominant Fourier coefficient is about 2.5 %, and our result again shows good agreement with the spectrum calculated from the result of Dunne and Rannacher (2006). Through the comparison with the other numerical methods, the validity of our method for the dynamic problem including the large deformation is confirmed.

Table 2: Simulation conditions for the flow around the elastic bar attached to the rigid cylinder.

fluid	Inflow average velocity	$\bar{U}$	$1 \, [\frac{m}{s}]$
	Density	ρ_f	$1 \times 10^3 \, [\frac{kg}{m^3}]$
	Dynamic viscosity	ν_f	$1 \times 10^{-3} \, [\frac{m^2}{s}]$
elastic body	Density	ρ_s	$1 \times 10^4 \, [\frac{kg}{m^3}]$
	Poisson's ratio	ν	0.4
	Lamé constant	μ	$5 \times 10^5 \, [\frac{kg}{ms^2}]$
numerical parameter	Time increment	Δt	$2.5 \times 10^{-5} [s]$
	Number of grid points for fluid	$N_x \times N_y$	1500×246
	Numbers of nodes and elements for solid	N_n, N_e	3853, 6720
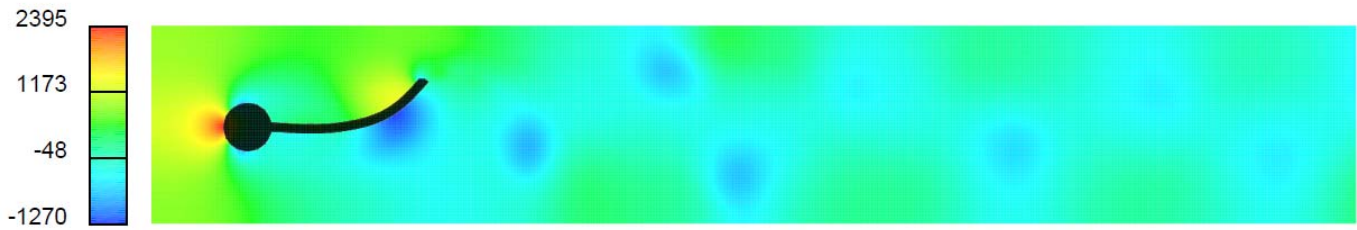
Figure 7: Snapshot of the deformed elastic object and contour of the pressure field.

5 Application to bio-related flows

5.1 The flow through the vocal cords

Vocal cords are vibrated by an expiratory flow and contacts of the vocal cords occur. Until now, various simple models for the flow through a model of vocal cords have been proposed (Story and Titze 1995; Flangan and Ishizaka 1978). However, only a few simulations have considerd a realistic vocal cords model and a realistic FSI (Šidlof 2007; Luo et al. 2008; Zheng et al. 2009). In this paper, the influences of a clearance of the vocal cords model at the initial condition (neutral shape) and the contact of the vocal cords on the vibration are investigated.

An actual vocal cords are composed of several layers of different bio-materials. For simplicity, we use a vocal cord model consisting of two layers (cover and body) of different Young's moduli. A St.Venant-Kirchhoff material is assumed for the elastic objects. The geometry of the pair of the vocal cords is depicted in Fig.10. In the figure, H equals half of D which is a channel width when there is no initial clearance (h). Figure 11 illustrates the computational domain and the boundary conditions for the flow through the elastic objects. The velocity profile of a sufficiently developed parallel flow is given at the inflow boundary. At the outflow section, the velocity boundary condition is a convective outflow proposed by Orlanski (1976). A sponge domain is located near the outflow boundary, where the mesh is stretched locally in the downstream direction (x) and a first order
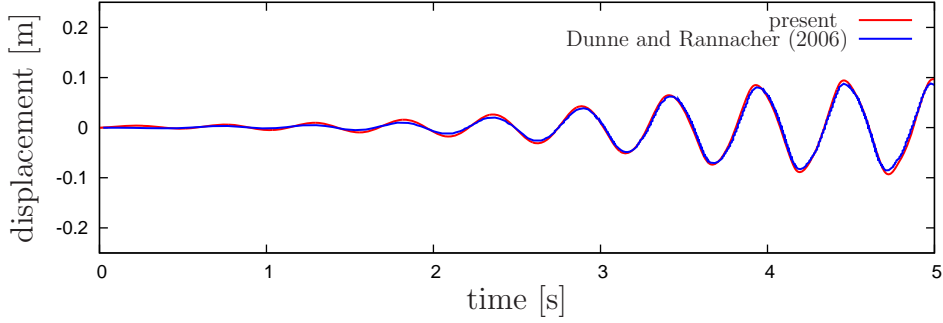
Figure 8: Time evolution of displacement in the y-direction at Point "A".
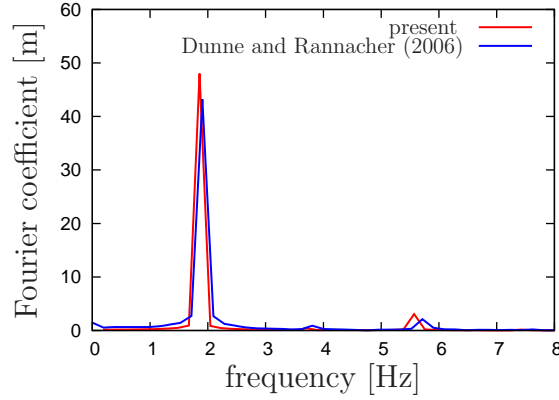

Figure 9: The Fourier coefficient of the elastic bar vibration at Point "A".

upwind scheme for the convective term in Eq.(2) is applied to diffuse strong vortices. At the top and bottom boundaries, the no-slip condition is imposed. Initially, $\boldsymbol{u} = 0$ is given in the entire domain. As for the boundary conditions for the elastic objects, the nodes on the rigid walls are fixed. The computational condition is shown in Tab.3. All the variables are non-dimensionalized by the averaged fluid velocity u_m and the channel width D with no clearance. Reynolds numbers are determined by changing the channel width (considering the clearance) while keeping the reference velocity and dynamic viscosity fixed, and given in Tab.3. The parenthesized elastic moduli in Tab.3 are dimensional values for reference under the conditions of $D = 2 \times 10^{-2}$[m] (based on the study of Luo et al. (2008)) and $\nu_f = 1.501 \times 10^{-5}$[m^2/s].

Two snapshots of the instantaneous flow fields through the elastic objects are shown in Fig.12 when the vocal cords are fully closed and open. From our observation, strong jet through the elastic objects is observed when the gap between the two objects is small at the opening and closing moments.

16
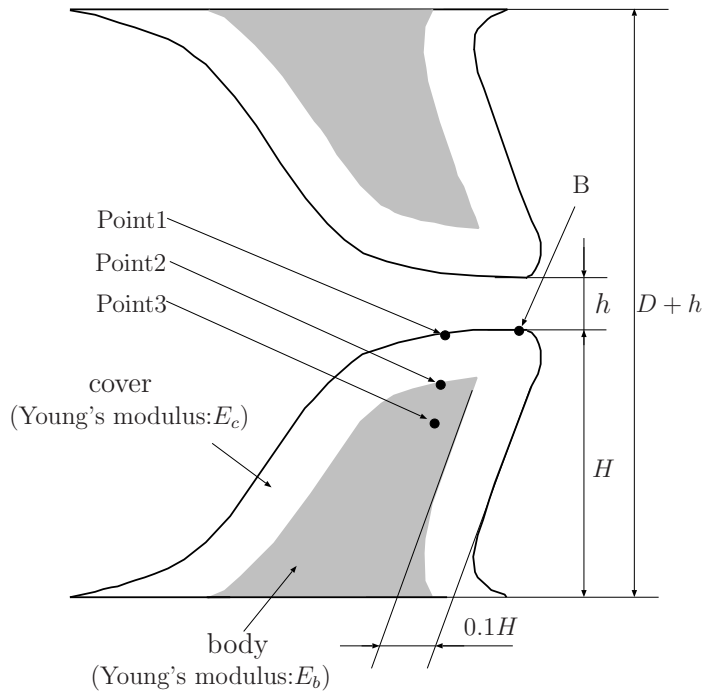
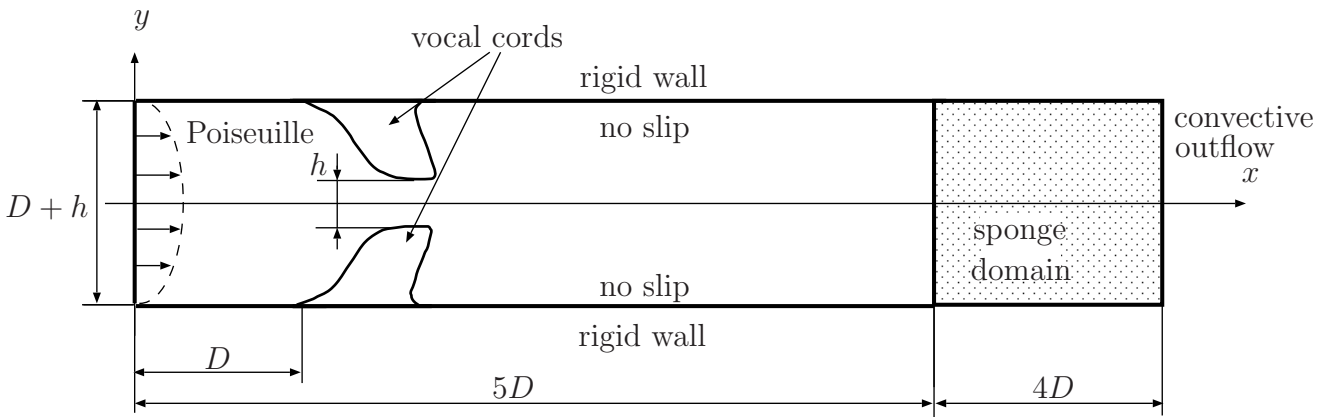Figure 10: A schematic of the vocal cords model.

Figure 11: The computational domain of the flow through the vocal cords model.

Consequently, the strong vortices are discharged behind the elastic objects as Fig.12 shows, and the symmetry of the flow field breaks in the immediate downstream of the vocal cords.

The influence of the initial clearance on the vocal cord vibration is studied. The results of the discrete Fourier transform of the vertical displacement of Point "B" on the surface (see Fig.10) are shown in Fig.13. From the figure, the frequencies of the strongest Fourier coefficient are classified into two modes in terms of values of the initial clearance. To analyze the dominant vibrating modes, an eigenmode analysis of the elastic object is performed by solving the linear equation:

$$\left| \boldsymbol{K} - \omega_n^2 \boldsymbol{M} \right| = 0, \tag{28}$$

where $\boldsymbol{K}$ and ω_n are the stiffness matrix and the n-th order eigen angular frequency, respectively. The first three eigenfrequencies ($f_n = \omega_n / 2\pi, n = 1, 2, 3$) are found to be 1.85, 4.12 and 5.45. When

Table 3: Simulation conditions for the flow through the vocal cords.

fluid	Reynolds number	$Re = Du_m/\nu_f$	$1500 \times (D+h)/D$
elastic object	Young's modulus of cover	E_c	5.0×10^4 (76[kPa])
	Young's modulus of body	E_b	1.0×10^5 (153[kPa])
	Density ratio	ρ_s/ρ_f	1.0×10^3
	Poisson's ratio	ν	0.2
numerical parameter	Time increment	Δt	5×10^{-5}
	Number of grid points	$N_x \times N_y$	$600 \times (100 + 100 \times h/D)$
	Numbers of nodes and elements	N_n, N_e	844, 1446
	Clearance	h/D	0, 0.01, 0.02, 0.04, 0.05
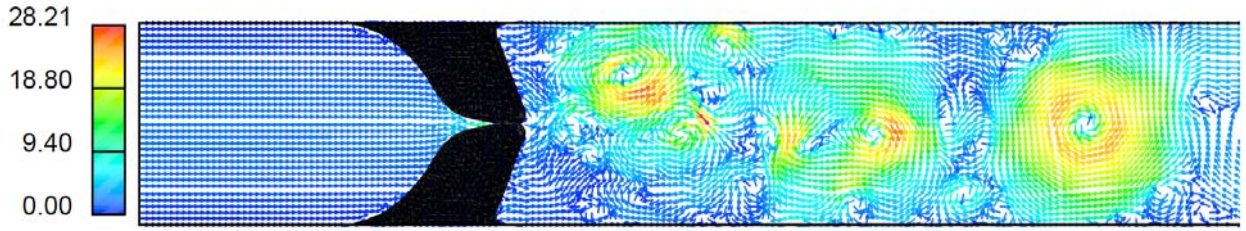
(a) closed state.
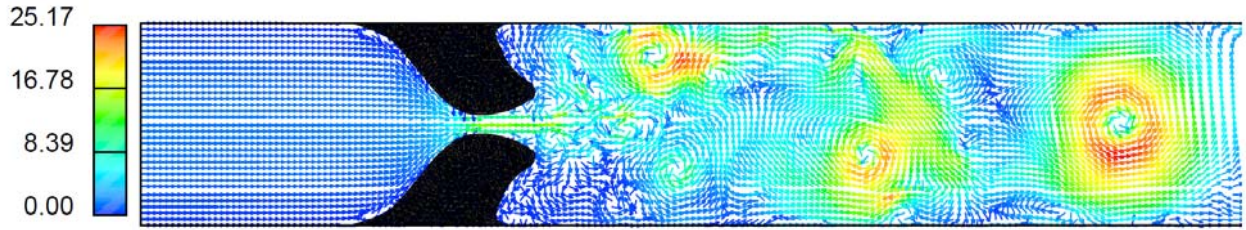
(b) opened state.

Figure 12: Instantaneous flow fields through the vocal cords. The magnitude of the velocity is color-coded.

the clearance of the elastic objects is small ($h = 0$, 0.01, 0.02), the dominant frequencies are close to the value of Mode 2 but slightly reduced probably due to the effect of hydrodynamic force. On the other hand, when the clearance is large ($h = 0.04$, 0.05), the frequencies are close to the values of Mode 1. From these results, to vibrate at a high frequency, a small or zero initial clearance of the elastic objects is desirable. To see the further differences of the two modes, Fig.14 plots the trajectories of the three Lagrangian points (Points 1, 2 and 3 in Fig.10) under the vibration when initial clearance is $h = 0.02$ or $h = 0.05$ together with the cheracteristic directions of Mode 1 and 2. The trajectories for the case of $h = 0.02$ are rather dispersed but show good agreement with the direction of Mode 1 (particularly near the surface of the object) although the frequency is close to Mode 2. On the other hand, the trajectories in the case of $h = 0.05$ show a sharp agreement with the direction of Mode 1. When the initial clearance is large, the vibration is close to the condition of the free oscillation because the fluid forces are small compared to the elastic and inertia forces on the elastic objects, and the lowest frequency (Mode 1) manifests itself.
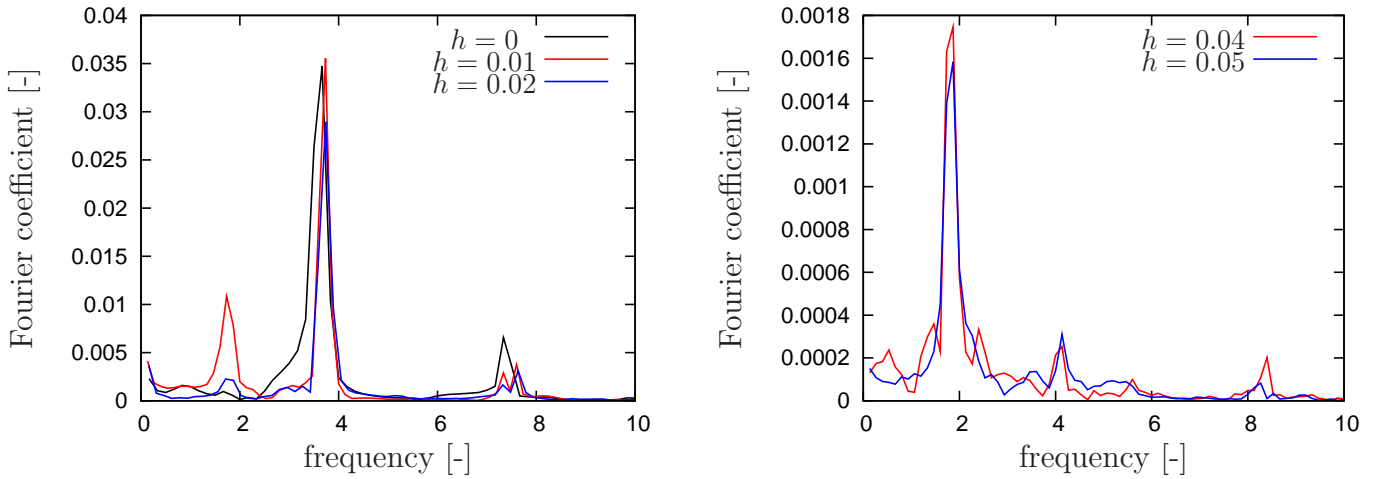
Figure 13: The Fouirer coefficients of the vocal cords vibration at Point "B".
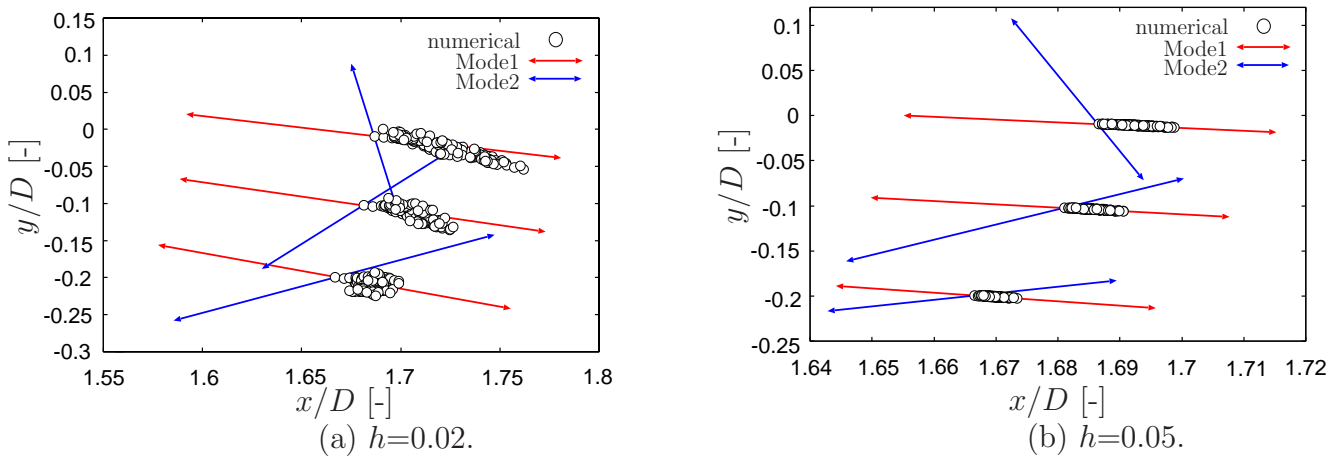

(a) h=0.02.   (b) h=0.05.

Figure 14: Trajectories of the structural vibration excited by the fluid and characteristic directions of Mode 1 and 2. Circles show the trajectories of the points of the structure.

We also study the influence of the contact force on the vocal cord vibration. The contacts take place when $h = 0$ and 0.01, and the clearance larger than $h = 0.02$ do not cause the full obstruction of the channel. In that case, the contacts do not necessarily play an important role for the vibration at high frequencies since the high frequency mode is also dominant when $h = 0.02$ (see Fig.13). Time evolution of the contact force and fluid force in the case of $h = 0$ (no clearance) at the initial condition is plotted in Fig.15. These forces are the sum of the equivalent nodal forces of the third and fifth terms in Eq.(5), respectively. The contact force is larger than the fluid force except while the contact continues. The impulse of the contact force is about ten times smaller than that of the fluid force since the duration of the contact is very short. This result of the force comparison also indicates that the contacts do not predominantly influence the frequencies of the elastic objects.
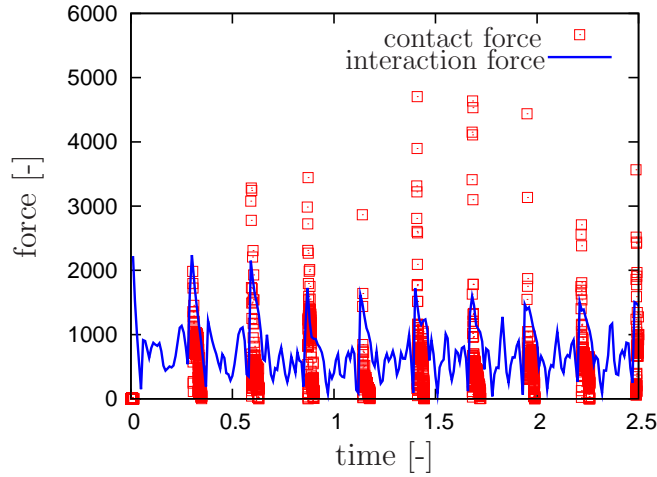
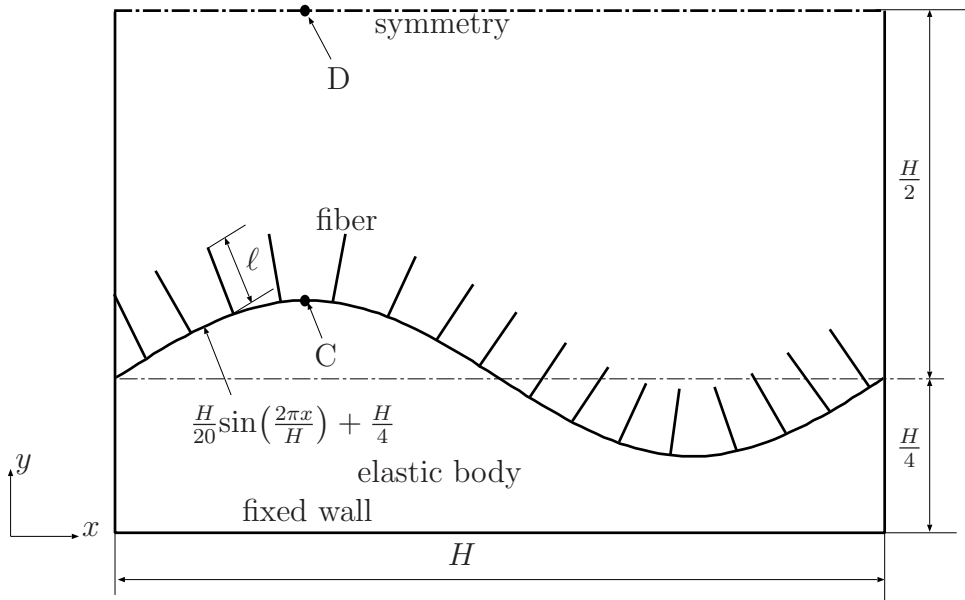Figure 15: Time evolution of the contact force and interaction force.

Figure 16: The computational domain for flow through the elastic channel with fibers.

5.2   The flow through the elastic channel with fibers

Glycocalyx is a flexible fiber-like sugar-chain placed on a blood vessel wall (van den Berg et al. 2003). In this section, the hydrodynamic effect by the presence of the fiber elements is investigated, as an example of fluid-structure interaction problem including the solids of different dimensional topologies.

The computational domain and boundary condition are schematically shown in Fig.16. Sixteen fibers are clamped on the elastic wall at regular intervals. For the fluid phase, the periodic condition is imposed on the left and right boundaries. The symmetric condition for the upper boundary ($\forall x, y = 3H/4$) and the no-slip condition for the lower boundary ($\forall x, y = 0$) are applied. For the elastic body, the left and right sides are periodic, and the displacement of the bottom nodes are fixed. A St.Venant-Kirchhoff material is assumed for the elastic wall. The fibers are put on the surface of

Table 4: Simulation parameters for the flow through the elastic channel with the fibers.

fluid	Reynolds number	Re_τ	25
	Young's modulus	E	10
elastic body	Poisson ratio	ν	0.2
	Density ratio	ρ_s/ρ_f	10
	Length	ℓ/H	0.125
fiber	Density ratio	ρ_f/ρ_f	1.1
	Bending stiffness	γ_f	10^{-4}
	Time increment	Δt	1.0×10^{-4}
	Number of grid points for fluid	$N_x \times N_y$	128×96
numeical parameter	Numbers of nodes and elements for elastic objects	N_n, N_e	1105, 2048
	Number of segments for fiber	n_{seg}	62
	Constant in Eq.(23)	κ	10^5

(a) $t = 7.1$ (b) $t = 7.7$
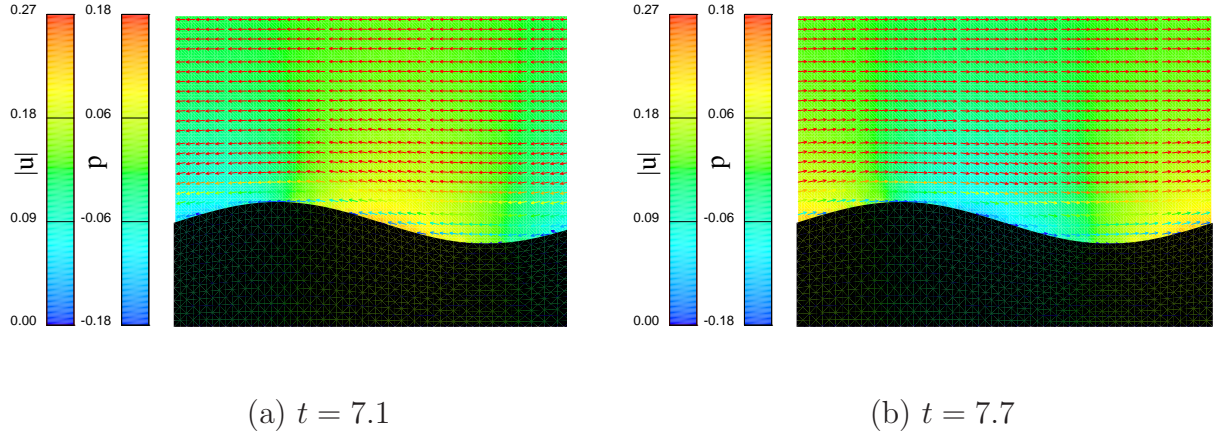
Figure 17: Pressure and velocity fields in case without the fibers on the rigid wall. The vector and contour show the vecloity and pressure, respectively.

the elastic body, and they are clamped at right angles at the points of the installation. To mimic a pulsation, the fluid is driven by a sinusoidally-varying pressure gradient in the x-direction as follows:

$$-\frac{\partial p}{\partial x} = \frac{2\tau_w}{H}\sin\left(\frac{2\pi t}{T}\right),$$ (29)

where τ_w and T are the wall shear stress and period of the driving force, respectively. The computational parameters are summarized in Tab.4. A frictional velocity and channel width is used for non-dimensionalization, and T is set to be 1.2.

The snapshots of the velocity and pressure fields under no-fiber condition on the rigid walls are shown in Fig.17. The times of the two snapshots are different by $T/2$, and the mainstream flow is in the opposite direction to each other. The local pressure and velocities vary due to a wavy shape of the channel. Pressure is high in the side facing the flow direction, and the pressure is low in the side not facing the flow direction. This tendency is also observed in the cases with the fibers on
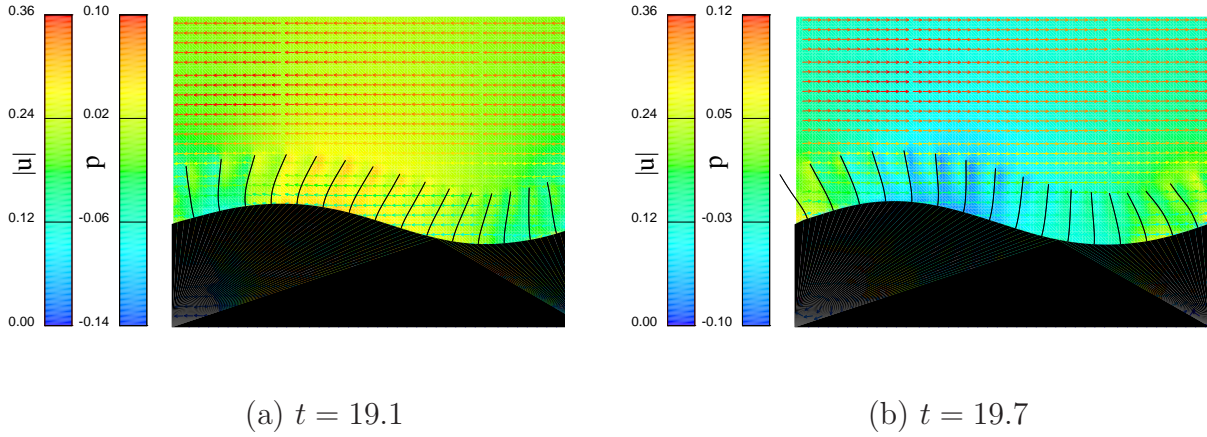
(a) $t = 19.1$ (b) $t = 19.7$

Figure 18: Pressure and velocity fields in case with the fibers on the elastic wall. The vector and contour show the vecloity and pressure, respectively.
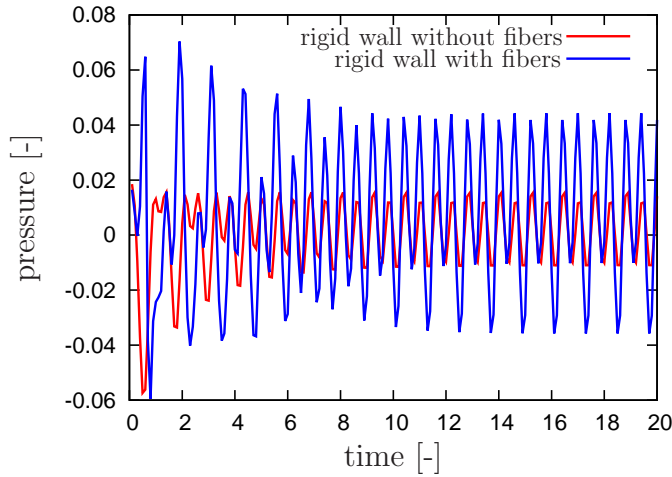

Figure 19: Time evolution of the pressure at Point "C".

the elastic wall as shown in Fig.18. The two snapshots are taken at half period interval when the magnitude of the centerline velocities becomes the strongest. The fibers move in the flow direction in both figures. The fluid velocities in the regions between the fibers are approximately aligned in the horizontal direction and the magnitudes are almost the same, while the pressures in the inter-fiber regions are different depending on the position of the elastic wall. Figure 19 shows a time evolution of the pressure at Point "C" (see Fig.16). The pressure fluctuation is small when there is no fiber since the normal direction at "C" is perpendicular to the flow direction. However, if there are fibers, the pressure fluctuation is large since the flow is interrupted by the fibers. Figure 20 shows a time evolution of the wall shear stress at Point "C". The wall shear stress is obtained by the following equation:

$$\tau_{\text{wall}} = \frac{2}{Re} \boldsymbol{t} \cdot \boldsymbol{D} \cdot \boldsymbol{n}, \tag{30}$$
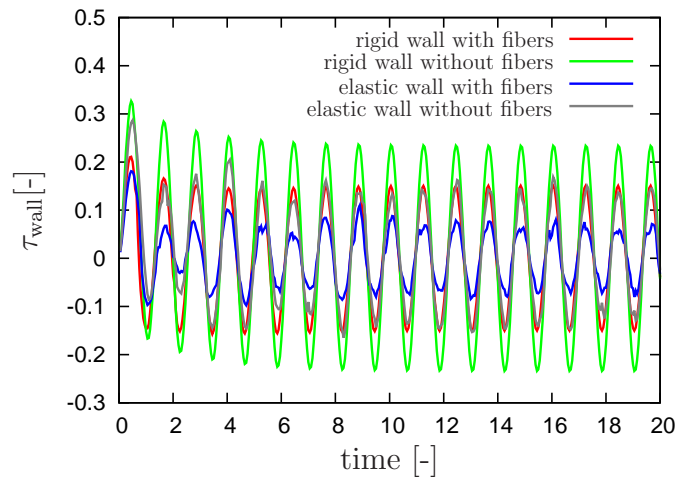
Figure 20: Time evolution of the wall shear stress at Point "C".

where t, n and D are the unit tangential vector, the unit normal vector and the deformation velocity tensor, respectively. In the figure, the wall shear stress in the presence of the fibers is small compared with that in the case without the fibers regardless of the rigid or elastic wall. This is because the velocity gradient on the wall becomes small due to the interruption of the flow by the fibers, as shown by the velocity profile in Fig.21. Also from Fig.20, the wall shear stress on the elastic wall is small compared with that on the rigid wall because the elastic wall moves at the same phase as the pulsation of the flow. The motions of the fluid and solid are also synchronized as observed in Fig.22 with the time evolutions of the centerline flow velocity and elastic wall velocity. The average amplitudes of the fluctuation of the flow rate are plotted in Fig.23. The flow rate in the presence of the fibers is small compared with that for the case without the fibers. The result suggests that the fibers resist the flow in compensation for the reduction of the wall shear stress. Also from the figure, the elasticity of wall helps increase the flow rate due to the synchronized motion of the fluid and solid, resulting in the reduction of the velocity gradient on the wall in the present cases. These results are obtained by considering the large deformations of the solid objects, and the simulation results show a wide applicability of our method for biological flows.
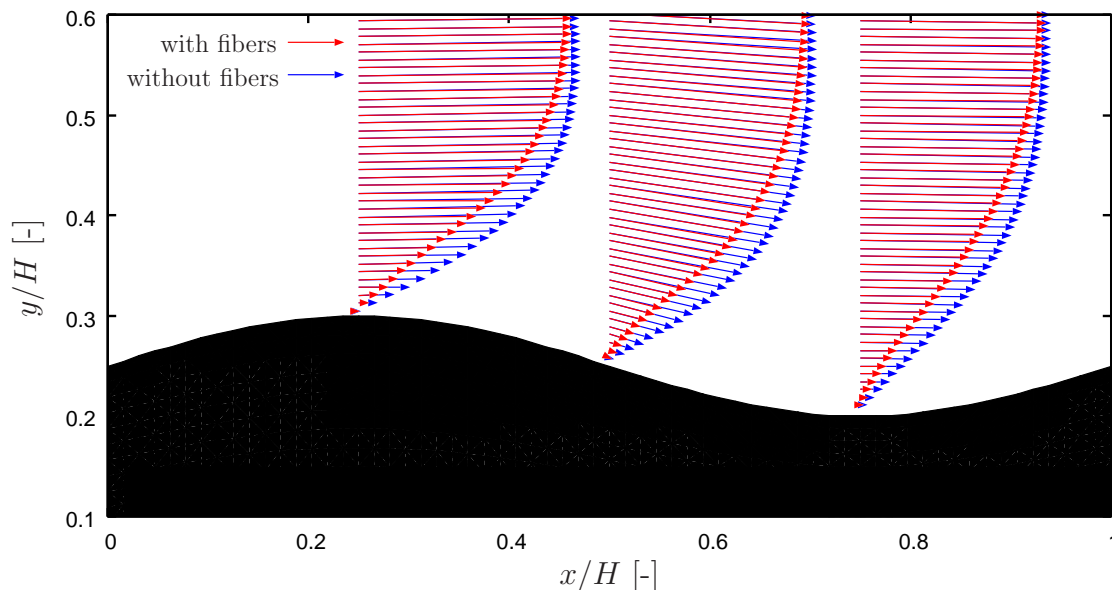
Figure 21: Comparison of the instantaneous velocity profiles at the moment of the smallest pressure gradient in the x-direction for the cases with fibers and without fibers on the rigid wall.
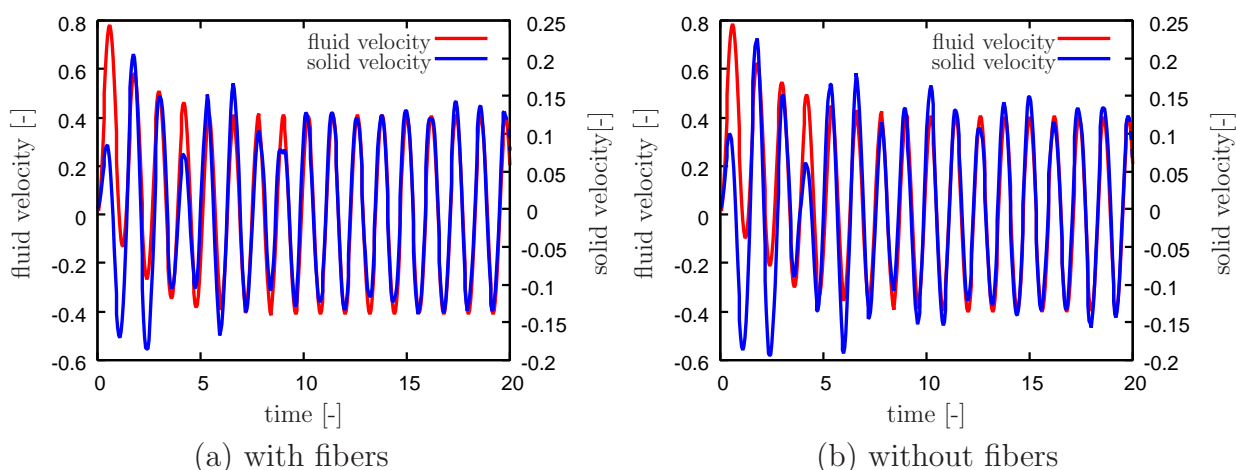

(a) with fibers

(b) without fibers

Figure 22: Time evolution of the fluid and solid velocities measured at Points "D" and "C", respectively (see Fig.16) for the cases with/without fibers.
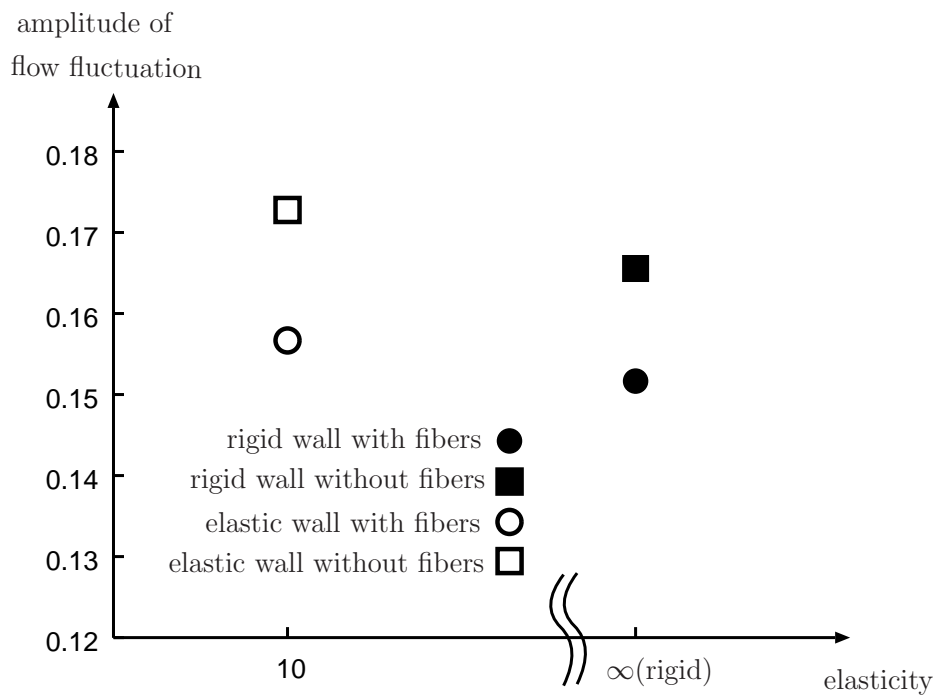
Figure 23: Amplitudes of the flow fluctuation at quasi-steady state against the elasticity of the wall.

6   Conclusion

We proposed a numerical method for fluid-structure interaction (FSI) problems, and applied to biological flows involving elastic objects of different dimensional topologies. Geometrical nonlinearity of the solids was considered to deal with the large deformation problems. Our scheme is composed of the three interaction models between the fluid, fibers and elastic objects with a finite volume. The immersed solid method and feedback immersed boundary method were coupled for the interaction between the fluid and solids of different dimensional topologies.

The validity of our method was established through comparisons to a static and dynamic FSI benchmark problems. Our method has a first order accuracy and the results of our method show good agreement with those by the other numrical methods.

The method was applied to two applications of biological flows. The first application was the flow through the vocal cords model, and the influences of an initial clearance of the vocal cords and the contacting of the vocal cords on the vibration were investigated. The vocal cords vibrations were found to be classified into two structural modes depending on the initial clearances of the vocal cords. The frequencies of the vocal cords are close to that of Mode 2 when the initial clearance is small, whereas the frequencies are close to that of Mode 1 when the initial clearance is large. The frequencies of the vocal cords vibration are almost the same whether the contacts between the vocal cords take place or not, suggesting that the contacts are not the primary factor in determining the frequencies of the vocal cords vibration.

The second application concerns the flow through the elastic channel with clamped fibers, and the hydrodynamic effect of the fiber elements on the flow and wall was investigated. Although the fibers act as a resistance for the flow, they were found to decrease the wall shear stress. The wall shear stress decreases further in the case including the elasticity of the wall. Therefore, considering the deformation of the solid objects is important for the reduction of the wall shear stress on the channel.

Our method is capable of handling a number of FSI problems involving the large deformation of the elastic objects of different dimensional topologies, and it is likely to be a powerful tool for challenging problems in biological flows.

References

Baaijens, F. P. (2001). A fictitious domain/mortar element method for fluid-structure interaction. International Journal for Numerical Methods in Fluids, 35(7), 743-761.

Bathe, K. J., Zhang, H., & Wang, M. H. (1995). Finite element analysis of incompressible and compressible fluid flows with free surfaces and structural interactions. Computers & Structures, 56(2), 193-213.

Belytschko, T., & Black, T. (1999). Elastic crack growth in finite elements with minimal remeshing. International Journal for Numerical Methods in Engineering, 45(5), 601-620.

van den Berg, B.M., Vink, H. and Spaan, J.A.E. (2003). The Endothelial Glycocalyx Protects Against Myocardial Edema. Circulation Research, 92(6), 592-594.

Cottet, G. H., Maitre, E., & Milcent, T. (2008). Eulerian formulation and level set models for incompressible fluid-structure interaction. ESAIM: Mathematical Modelling and Numerical Analysis, 42, 471-492.

Dunne, T., & Rannacher, R. (2006). Adaptive finite element approximation of fluid-structure interaction based on an Eulerian variational formulation. Fluid-Structure Interaction. Springer Berlin Heidelberg. 110-145.

Flanagan, J. L., & Ishizaka, K. (1978). Computer model to characterize the air volume displaced by the vibrating vocal cords. The Journal of the Acoustical Society of America, 63, 1559. Anunals of biomedical engineering, 37(3), 625-642.

Gao, T., & Hu, H. H. (2009). Deformation of elastic particles in viscous shear flow. Journal of Computational Physics, 228(6), 2132-2151.

Gerstenberger, A., & Wall, W. A. (2008). An extended finite element method/Lagrange multiplier based approach for fluid-structure interaction. Computer Methods in Applied Mechanics and Engineering, 197(19), 1699-1714.

Glowinski, R., Pan, T. W., Hesla, T. I., & Joseph, D. D. (1999). A distributed Lagrange multiplier/fictitious domain method for particulate flows. International Journal of Multiphase Flow, 25(5), 755-794.

Goldstein, D., Handler, R., & Sirovich, L. (1993). Modeling a no-slip flow boundary with an external force field. Journal of Computational Physics, 105(2), 354-366.

Hübner, B., Walhorn, E., & Dinkler, D. (2004). A monolithic approach to fluid-structure interaction using space-time finite elements. Computer Methods in Applied Mechanics and Engineering, 193(23), 2087-2104.

Heil, M., Hazel, A. L.,& Boyle, J. (2008). Solvers for large-displacement fluid-structure interaction problems: segregated versus monolithic approaches. Computational Mechanics, 43(1), 91-101.

Huang, W. X., & Sung, H. J. (2009). An immersed boundary method for fluid-flexible structure interaction. Computer Methods in Applied Mechanics and Engineering, 198(33), 2650-2661.

Huang, W. X., Shin, S. J., & Sung, H. J. (2007). Simulation of flexible filaments in a uniform flow by the immersed boundary method. Journal of Computational Physics, 226(2), 2206-2228.

Ii, S., Sugiyama, K., Takeuchi, S., Takagi, S., & Matsumoto, Y. (2011). An implicit full Eulerian method for the fluid-structure interaction problem. International Journal for Numerical Methods in Fluids, 65(13), 150-165.

Ii, S., Gong, X., Sugiyama, K., Wu, J., Huang, H., & Takagi, S. (2012). A full Eulerian fluid-membrane coupling method with a smoothed volume-of-fluid approach. Communications in Computational Physics, 12(2), 544.

Ii, S., Sugiyama, K., Takagi, S., & Matsumoto, Y. (2012). A computational blood flow analysis in a capillary vessel including multiple red blood cells and platelets. Journal of Biomechanical Science and Engineering, 7(1), 72-83.

Kajishima, T., Takiguchi, S., Hamasaki, H., & Miyake, Y. (2001). Turbulence structure of particle-laden flow in a vertical plane channel due to vortex shedding. JSME International Journal Series B, 44(4), 526-535.

Kajishima, T., & Takiguchi, S. (2002). Interaction between particle clusters and particle-induced turbulence. International Journal of Heat and Fluid Flow, 23(5), 639-646.

Kim, Y., & Peskin, C. S. (2006). 2-D parachute simulation by the immersed boundary method. SIAM Journal on Scientific Computing, 28(6), 2294-2312.

Lee, L., & LeVeque, R. J. (2003). An immersed interface method for incompressible Navier-Stokes equations. SIAM Journal on Scientific Computing, 25(3), 832-856.

Li. Z.(1994) The immersed interface method: A numerical approach to partial differential equations with interfaces. Ph.D. thesis, Department of Applied Mathematics, University of Washington, Seattle, WA

Li, Z. (1997). Immersed interface methods for moving interface problems. Numerical Algorithms, 14(4), 269-293.

Liu, W. K., Jun, S., & Zhang, Y. F. (1995). Reproducing kernel particle methods. International Journal for Numerical Methods in Fluids, 20(8-9), 1081-1106.

Luo, H., Mittal, R., Zheng, X., Bielamowicz, S. A., Walsh, R. J., & Hahn, J. K. (2008). An immersed-boundary method for flow-structure interaction in biological systems with application to phonation. Journal of computational physics, 227(22), 9303-9332.

Mittal, R., & Iaccarino, G. (2005). Immersed boundary methods. Annual Review of Fluid Mechanics, 37, 239-261.

Moës, N., Dolbow, J., & Belytschko, T. (1999). A finite element method for crack growth without remeshing. International Journal for Numerical Methods in Engineering, 46, 131-150.

Mori, Y., & Peskin, C. S. (2008). Implicit second-order immersed boundary methods with boundary mass. Computer methods in applied mechanics and engineering, 197(25), 2049-2067.

Nagano, N., Sugiyama, K., Takeuchi, S., II, S., Takagi, S., & Matsumoto, Y. (2010). Full-Eulerian finite-difference simulation of fluid flow in hyperelastic wavy channel. Journal of Fluid Science and Technology, 5(3), 475-490.

Orlanski, I. (1976). A simple boundary condition for unbounded hyperbolic flows. Journal of Computational Physics, 21(3), 251-269.

Peskin, C. S., & Printz, B. F. (1993). Improved volume conservation in the computation of flows with immersed elastic boundaries. Journal of Computational Physics, 105(1), 33-46.

Peskin, C. S. (1977). Numerical analysis of blood flow in the heart. Journal of Computational Physics, 25(3), 220-252.

Peskin, C. S. (2002). The immersed boundary method. Acta numerica, 11(0), 479-517.

Sawada, T., & Hisada, T. (2007). Fluid-structure interaction analysis of the two-dimensional flag-in-wind problem by an interface-tracking ALE finite element method. Computers & fluids, 36(1), 136-146.

Sawada, T., Tezuka, A., Hisada, T. (2008). Performance comparison between the fluid-shell coupled overlaying mesh method and the immersed boundary method. Transactions of JSCES, No.20080005, pp.1-14 (in Japanese).

Sawada, T. (2006). Study of the overlaying ALE mesh computations of fluid-structure interaction problems. Ph.D. thesis, The University of Tokyo (in Japanese).

Šidlof, P. (2007). Fluid-structure interaction in human vocal folds. Doctoral dissertation, ENSTA ParisTech.

Stockie, J. M. (1997). Analysis and computation of immersed boundaries, with application to pulp fibres. Doctoral dissertation, University of British Columbia.

Story, B. H., & Titze, I. R. (1995). Voice simulation with a body-cover model of the vocal folds. The Journal of the Acoustical Society of America, 97, 1249.

Sugiyama, K., Ii, S., Takeuchi, S., Takagi, S., & Matsumoto, Y. (2010). Full Eulerian simulations of biconcave neo-Hookean particles in a Poiseuille flow. Computational Mechanics, 46(1), 147-157.

Sugiyama, K., Ii, S., Takeuchi, S., Takagi, S., & Matsumoto, Y. (2011). A full Eulerian finite difference approach for solving fluid-structure coupling problems. Journal of Computational Physics, 230(3), 596-627.

Takeuchi, S., Yuki, Y., Ueyama, A., & Kajishima, T. (2010). A conservative momentum-exchange algorithm for interaction problem between fluid and deformable particles. International Journal for Numerical Methods in Fluids, 64(10-12), 1084-1101.

Tezduyar, T. E., Behr, M., & Liou, J. (1992). A new strategy for finite element computations involving moving boundaries and interfaces-the DSD/ST procedure: I. The concept and the preliminary numerical tests. Computer Methods in Applied Mechanics and Engineering, 94(3), 339-351.

Tezduyar, T. E., Behr, Mittal, S., & Liou, J. (1992). A new strategy for finite element computations involving moving boundaries and interfaces-the deforming-spatial-domain/space-time procedure: II. Computation of free-surface flows, two-liquid flows, and flows with drifting cylinders. Computer Methods in Applied Mechanics and Engineering, 94(3), 353-371.

Tezduyar, T. E. (1992). Stabilized finite element formulations for incompressible flow computations. Advances in Applied Mechanics, 28, 1-44.

Tezduyar, T. E., Sathe, S., Keedy, R., & Stein, K. (2006). Space-time finite element techniques for computation of fluid-structure interactions. Computer Methods in Applied Mechanics and Engineering, 195(17), 2002-2027.

Turek, S., & Hron, J. (2006). Proposal for numerical benchmarking of fluid-structure interaction between an elastic object and laminar incompressible flow. Fluid-Structure Interaction. Springer Berlin Heidelberg. 371-385.

Van Loon, R., Anderson, P. D., De Hart, J., & Baaijens, F. P. (2004). A combined fictitious domain/adaptive meshing method for fluid-structure interaction in heart valves. International Journal for Numerical Methods in Fluids, 46(5), 533-544.

Wang, X., & Liu, W. K. (2004). Extended immersed boundary method using FEM and RKPM. Computer Methods in Applied Mechanics and Engineering, 193(12), 1305-1321.

Wiegmann, A., & Bube, K. P. (2000). The explicit-jump immersed interface method: finite difference methods for PDEs with piecewise smooth solutions. SIAM Journal on Numerical Analysis, 37(3), 827-862.

Wriggers, P. (2006). Computational contact mechanics second edition, Springer

Xu, S., & Wang, Z. J. (2006). An immersed interface method for simulating the interaction of a fluid with moving boundaries. Journal of Computational Physics, 216(2), 454-493.

Yuki, Y., Takeuchi, S., & Kajishima, T. (2007). Efficient immersed boundary method for strong interaction problem of arbitrary shape object with the self-induced flow. Journal of Fluid Science and Technology, 2(1), 1-11.

Zhang, Q., & Hisada, T. (2004). Studies of the strong coupling and weak coupling methods in FSI analysis. International Journal for Numerical Methods in Engineering, 60(12), 2013-2029.

Zhang, L., Gerstenberger, A., Wang, X., & Liu, W. K. (2004). Immersed finite element method. Computer Methods in Applied Mechanics and Engineering, 193(21), 2051-2067.

Zheng, X., Bielamowicz, S., Luo, H., & Mittal, R. (2009). A computational study of the effect of false vocal folds on glottal flow and vocal fold vibration during phonation. Anunals of biomedical engineering, 37(3), 625-642.

Zilian, A., & Legay, A. (2008). The enriched space-time finite element method (EST) for simultaneous solution of fluid-structure interaction. International Journal for Numerical Methods in Engineering, 75(3), 305-334.

Acknowledgments